ACS OMEGA

http://pubs.acs.org/journal/acsodf

Article

Real Gas Effect and Bulk Diffusion Characteristics of Shale Mixed Gas Transport in Microscale Fractures

Ying Yang, Xin Zhang, Xiaofeng Zhou, Anlun Wang, and Jiangtao Li*

Cite This: *ACS Omega* 2023, 8, 17077−17085

Read Online

ACCESS | Metrics & More | Article Recommendations

ABSTRACT: Shale gas reservoirs are rich in microscale fractures. In this paper, the characteristics of gas percolation in microscale fractures are taken as the research object. By coupling the actual gas equation, the multi-component gas equation, and the bulk gas diffusion equation, analytical solutions of the comprehensive percolation equation are obtained. Through mathematical model research, the following conclusions are obtained: (a) after considering the slip flow of the solid surface, the mass flow rate of multi-component gas under different pressure conditions increases by about 20−10,000%. (b) Different from continuous flow and slip flow, the mass flow rate of bulk gas diffusion decreases with pressure increase. (c) The intersection pressure is 31 MPa. When the pressure increases from 0.5 MPa to the pressure at the intersection point, the mass flow rate of integrated flow increases with decrease of the methane content. (d) When the pressure continues to increase from the intersection point pressure, the mass flow rate of integrated flow decreases with decrease of the methane content.

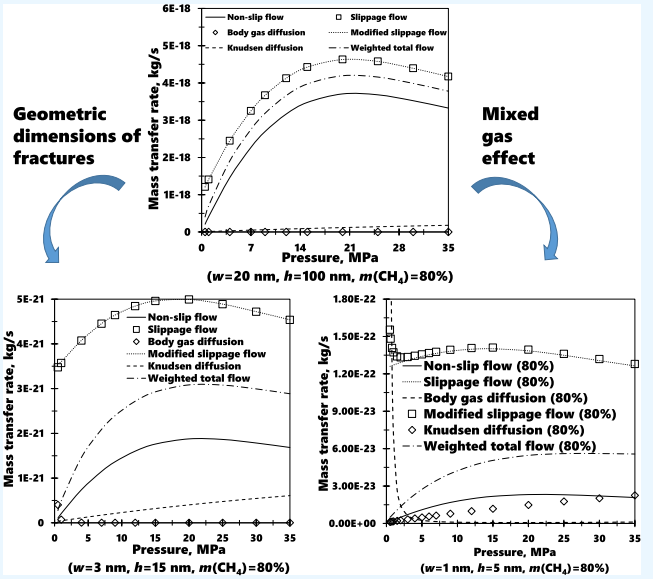

1. INTRODUCTION

1.1. Literature Review. Shale gas is quietly changing the global energy landscape.[1,2] Shale gas has the characteristics of wide distribution, abundant reserves, high efficiency and cleanliness, and great development potential.[3] Therefore, large-scale commercial development is bound to change the energy structure of the entire world[4] and even affect the global economy, geopolitics, and military structure.[5] According to statistics from U.S. Energy Information Administration in 2023:[6] China's total shale gas reserves are 144 trillion cubic meters, accounting for 20% of the world's total reserves.[7,8]

Although China has abundant shale gas reserves, shale gas development started later than the United States and Canada.[9] In 2015, China has formed Fuling, Changning-Weiyuan, and Yanchang shale gas production areas, with a total production capacity of 7.5 billion cubic meters.[5,10] The proportion in the energy structure reaches about 10%.[10,11] Methane is mainly stored in dark or high-carbon shale in free and adsorbed state.[12−15] Shale gas reservoir in the United States is 1000−3000 m deep, and the surface is mostly plain.[16] The porosity of shale core analysis in major producing areas in the United States is 2.0 to 14.00%, with an average of 4.22 to 6.51%;[17] the permeability is 1 nD−1 mD.[18−24] Many scholars have carried out a lot of research from the perspectives of experimental testing, micro-observation, and model establishment.[25−28] The matrix has a wide pore size distribution, rich organic matter content, and complex shale pore structure.[29−31] Zhang et al.[32] studied samples taken from two shale reservoirs and one coal reservoir in the United States. Wang et al.[33] found that the gas adsorption volume is 0.94−4.29 cm^3/g. Wang et al.[34] found that the maximum absolute adsorption capacity is between 0.50 and 3.41 cm^3/g. Chen et al.[35] and Zhao et al.[36] studied the adsorption characteristics in shale nanoscale pores through molecular dynamics simulation. Li et al.[37] experimentally studied and predicted Langmuir adsorption pressure and volume through comprehensive polynomial simulations. Chen et al.[38] studied the adsorption characteristics of Longmaxi shale through a specific gravity test method.[39] Due to large micro-porosity and high specific surface area of organic matter, the methane

Received: March 1, 2023
Accepted: April 20, 2023
Published: May 1, 2023

adsorption content also increases with the increase of the TOC content.[40−46] Loucks et al.[47] conducted a further detailed study on the pore structure types of shale and plotted the pore structure spectrum. Zou et al.[17] used field emission electron microscope scanning combined with the Nano-CT technology to discover the microscale pore structure in the shale reservoirs in the Sichuan Basin in China for the first time. Yang et al.[48] classified the pores in shale reservoirs into five categories through scanning electron microscopy. Yang et al.[24] calculated the fractal dimensions of shale samples through nitrogen adsorption experimental data. Since then, many scholars[49−52] have quantitatively described the relationship between the shale mineral composition and pore structure of different reservoirs through fractal characteristics. Sakhaee-Pour and Bryant[53] established a non-cyclic shale pore structure model. Sun et al.[54,55] used the Markov Chain Monte Carlo method and SEM images to obtain a digital core characterizing the three-dimensional pore structure of the shale matrix. Hou[56] used a field emission electron probe micro-analyzer and a high-resolution three-dimensional X-ray microscopic imaging system to reconstruct the shale matrix in three dimensions. Javadpour et al.[22] used 152 cores from nine shale gas reservoirs in North America to conduct a pulse decay permeability test. Many scholars[57−60] in the field of physical chemistry have carried out detailed research on the flow of gas in microscale tubes. Klinkenberg[61] and Beskok and Karniadakis[62] proposed a model that can simultaneously couple four flow mechanisms in one equation. Civan[63] made further corrections to the rarefied coefficient and gas slip coefficient.[64] Darabi[65] revised the Singh et al.[66] studied gas flow characteristics in microscale tubes, linearly superimposed diffusion and convection flux. Wu et al.[67] and Xiong et al.[68] believed that the presence of adsorbed methane on the pore surface narrowed the porosity and the pores for free phase gas transport. Wu et al.[69] established a mathematical model of shale gas surface diffusion. Many scholars[70−78] consider different factors and derive a large number of apparent permeability models through various methods.[26,79] Liu[26] conducts in-depth research on the multi-scale gas migration model and the cooperative mechanism of the migration process under the condition of multi-physics coupling.

1.2. Summaries. In summary, the combination of complex reservoir characteristics and nanoscale pore size makes the gas migration behavior in porous shale extremely complicated. During the development of shale gas reservoirs, the apparent permeability/diffusion rate model that accurately characterizes the gas migration in nanoscale pores is essential for the establishment of a macroscopic model. As a result, it is necessary to study the multi-component, multi-scale, and multi-migration mechanism of the matrix, reveal the complex migration mechanism of gas in the shale matrix, and effectively guide the practice of shale gas production. In summary, the combination of complex reservoir characteristics and nanoscale pore size makes the gas migration behavior in porous shale extremely complicated. During the development of shale gas reservoirs, the apparent permeability/diffusion rate model that accurately characterizes the gas migration in nanoscale pores is essential for the establishment of a macroscopic model. Therefore, it is necessary to study the multi-component, multi-scale, and multi-migration mechanism of the matrix, reveal the complex migration mechanism of gas in the shale matrix, and effectively guide the practice of shale gas production.

2. NOVELTIES OF THIS PAPER

In this paper, the fluid seepage in microscale fractures in shale gas formations is studied. The model considers the geometric characteristics of the fracture and also considers the real gas effect and the mechanism of bulk gas percolation. On the basis of model verification, the influence of fracture geometry and methane content on the percolation of mixed gas is analyzed.

3. ANALYTICAL MODEL

Considering the coupling influence mechanism of "multi-element gas effect—bulk gas effect—high pressure effect", the analytical equations for microscale gas flow are established as eqs 1 and 2. The detailed derivation process of eqs 1 and 2 can be found in Appendix A.

$$
\begin{aligned}
J_{t,real} &= \left[1 + \frac{\lambda_{real,mixture}}{r_{equivalent}}\frac{(1 + 1/\varsigma)}{2}\right]^{-1} J_{vsb,real} \\
&\quad + \left[1 + \frac{r_{equivalent}}{\lambda_{real,mixture}}\frac{2}{1 + 1/\varsigma}\right]^{-1} J_{k,real} \\
&= \left[1 + \frac{\lambda_{real,mixture}}{r_{equivalent}}\frac{(1 + 1/\varsigma)}{2}\right] \\
&\quad \left[-A(\varsigma)\frac{\phi}{\tau}\frac{wh^3}{12\mu_{real,mixture}}\frac{pM_{mixture}}{Z_{mixture}RT}\right. \\
&\quad (1 + \alpha Kn_{real,mixture}) \\
&\quad \left(1 + \frac{6Kn_{real,mixture}}{1 - bKn_{real,mixture}}\right)\frac{dP}{dl} \\
&\quad + \frac{1}{Kn_{real,mixture}}\left(-\frac{1}{3}\varsigma\lambda_{real,mixture}\sigma^{D_f - 2}\right. \\
&\quad \left.\left.\left(\frac{8ZM_{mixture}}{\pi RT}\right)^{0.5}\frac{P}{Z_{mixture}}C_g\frac{dP}{dL}\right)\right] \\
&\quad + \left[1 + \frac{r_{equivalent}}{\lambda_{real,mixture}}\frac{2}{1 + 1/\varsigma}\right]\left[-B(\varsigma)\frac{\phi}{\tau}\left(\frac{wh}{\pi}\right)^{3/2}\right. \\
&\quad \left(\frac{Z_{mixture}M_{mixture}}{2\pi TR}\right)^{1/2}\frac{P}{Z_{mixture}} \\
&\quad \left.\left(\frac{1}{P} - \frac{1}{Z_{mixture}}\frac{dZ_{mixture}}{dP}\right)\frac{dP}{dl}\right]
\end{aligned}
\tag{1}
$$

Conductivity

https://doi.org/10.1021/acsomega.3c01391
ACS Omega 2023, 8, 17077−17085

$$
\begin{aligned}
C_{t,\mathrm{real}} &= \left[1 + \frac{\lambda_{\mathrm{real,mixture}}}{r_{\mathrm{equivalent}}}\frac{(1 + 1/\varsigma)}{2}\right]^{-1} J_{\mathrm{vsb,real}} \\
&\quad + \left[1 + \frac{r_{\mathrm{equivalent}}}{\lambda_{\mathrm{real,mixture}}}\frac{2}{1 + 1/\varsigma}\right]^{-1} J_{k,\mathrm{real}} \\
&= \left[1 + \frac{\lambda_{\mathrm{real,mixture}}}{r_{\mathrm{equivalent}}}\frac{(1 + 1/\varsigma)}{2}\right] \\
&\quad \left[- A(\varsigma)\frac{\phi}{\tau}\frac{wh^3}{12\mu_{\mathrm{real,mixture}}}\frac{pM_{\mathrm{mixture}}}{Z_{\mathrm{mixture}}RT} \right. \\
&\quad (1 + \alpha Kn_{\mathrm{real,mixture}}) \\
&\quad \left(1 + \frac{6Kn_{\mathrm{real,mixture}}}{1 - bKn_{\mathrm{real,mixture}}}\right) \\
&\quad + \frac{1}{Kn_{\mathrm{real,mixture}}}\left(-\frac{1}{3}\varsigma\lambda_{\mathrm{real,mixture}}\sigma^{D_f - 2}\right. \\
&\quad \left.\left.\left(\frac{8ZM_{\mathrm{mixture}}}{\pi RT}\right)^{0.5}\frac{P}{Z_{\mathrm{mixture}}}C_{\mathrm{g}}\right)\right] \\
&\quad + \left[1 + \frac{r_{\mathrm{equivalent}}}{\lambda_{\mathrm{real,mixture}}}\frac{2}{1 + 1/\varsigma}\right]\left[-B(\varsigma)\frac{\phi}{\tau}\left(\frac{wh}{\pi}\right)^{3/2}\right. \\
&\quad \left(\frac{Z_{\mathrm{mixture}}M_{\mathrm{mixture}}}{2\pi TR}\right)^{1/2}\frac{P}{Z_{\mathrm{mixture}}} \\
&\quad \left.\left(\frac{1}{P} - \frac{1}{Z_{\mathrm{mixture}}}\frac{\mathrm{d}Z_{\mathrm{mixture}}}{\mathrm{d}P}\right)\right]
\end{aligned} \tag{2}
$$

4. RESULTS AND DISCUSSION

4.1. Parameter Values. By using eqs 1 and 2, the microscale transport mechanism of multi-component gas in microscale fracture is analyzed. A table with detailed calculation parameters is shown below (Table 1).

Table 1. Detailed Calculation Parameters

parameters	value
shale matrix porosity	0.0229
shale reservoir temperature	477 K
rare effect coefficient when $Kn \to \infty$	1.20
fitting constant α_1	3.8
fitting constant β	0.502
gas slip constant b	−1.02
fractal dimension of shale microscale fracture wall	2.08
fitting constant A_1	7.7581
fitting constant A_2	0.00000900254689
fitting constant A_3	0.309875

4.2. Influence of Crack Size on the Transmission Rate. Microscale fractures are widely developed in shale and coal rocks. The geometric characteristics of microscale fractures have a significant impact on fluid migration characteristics. The methane content is set as 80% and kept unchanged. The ratio of crack opening to height is set as 20 nm:100 nm, 3 nm:15 nm, and 1 nm:5 nm.

It can be found from Figure 1 that (a) micro-fractures have an important impact on shale gas bearing property and seepage capacity. The opening and closing state of micro-fractures is critical to the influence of shale gas-bearing. The percolation capacity is also an important factor to evaluate the physical properties of shale reservoirs. (b) Shale is a typical ultra-low permeability reservoir. The foliation fractures in micro-scale fractures extend far along the bedding plane, which can effectively improve the permeability of shale reservoirs. Quantitative characterization of the percolation capacity of micro-fractures is of great significance for shale reservoir physical property evaluation. At the same time, the permeability of shale reservoirs is very sensitive to the change of effective stress. In the process of hydrocarbon generation and expulsion and shale gas development, the reservoir permeability may change for several orders of magnitude. (c) It should be noted that compressibility factor and average molecular weight are used to simulate the mixed gas in this paper, as shown in Appendix A. The correctness of the compressibility factor and average molecular-weight calculation is proved by the verification of the comprehensive model.

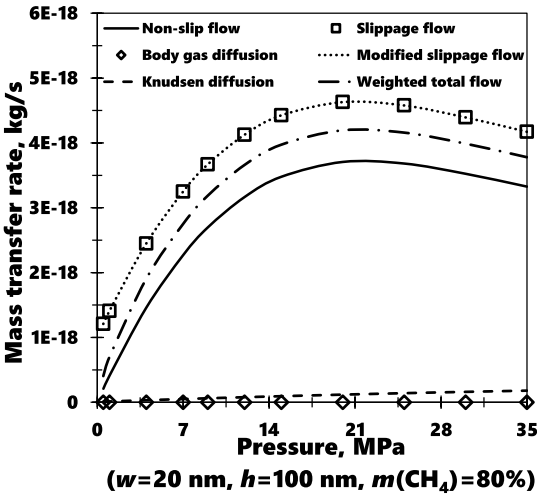

Figure 1. Relationship between mass flow rates of different seepage mechanisms and pressure when the fracture width is 20 nm and fracture height is 100 nm.

Figure 2 shows that the shale permeability gradually decreases with increase of effective pressure, and the micro-fracture gradually closes, but its reduction rate gradually slows down. In the process of micro-crack closure, there are mainly three stages. The first stage is the rapid decline of permeability, during which the opening of micro-fractures decreases, and the originally narrow parts of the fractures contact with each other, leading to the rapid reduction of permeability, which is the most important factor of permeability reduction. The opening of microscale fractures is further reduced, and a large number of originally narrow parts are further closed. Micro-fractures are divided into discontinuous spaces. The mechanical compaction of mineral particles, the reduction of intergranular pores, and the closure of micro-fractures occur simultaneously. The third stage is the constant stage of permeability. The permeability is only slightly reduced or tends to be stable, and the compressible space in shale has basically disappeared at the third stage.

Figure 3 shows that average proportion of microscale pore-fracture volume in shale reservoir can reach more than 20%, which is an important part of shale reservoir space. Micro-fractures in micro-scale fractures can provide certain pore volume for shale reservoirs and are an important type of reservoir space in shale. Micro-fractures can promote the

https://doi.org/10.1021/acsomega.3c01391
ACS Omega 2023, 8, 17077−17085

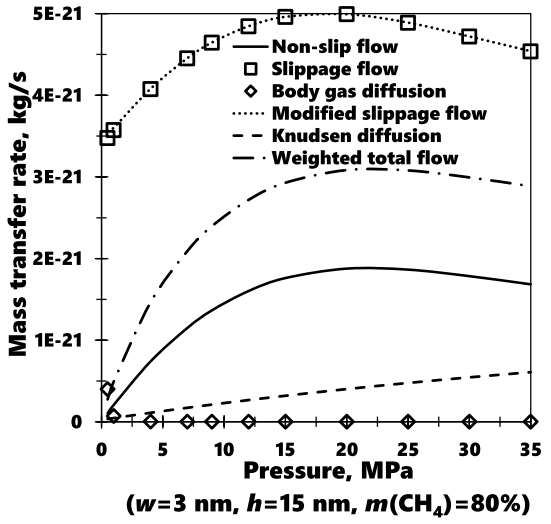

Figure 2. Relationship between mass flow rates of different seepage mechanisms and pressure when the fracture width is 3 nm and fracture height is 15 nm.

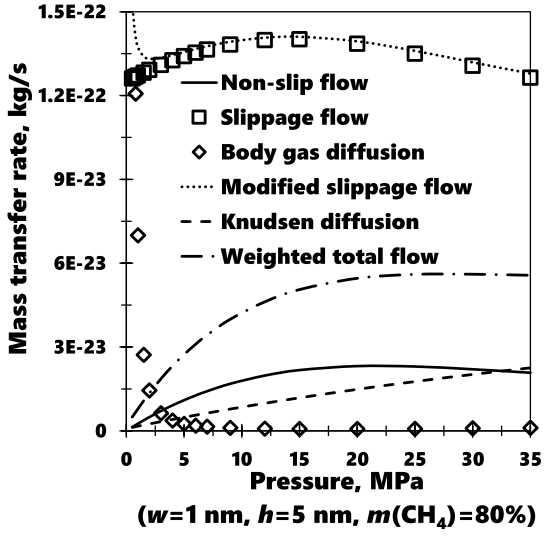

Figure 3. Relationship between mass flow rates of different seepage mechanisms and pressure when the fracture width is 1 nm and fracture height is 5 nm.

transformation of adsorbed shale gas into free shale gas in the shale reservoir, thus keeping the shale reservoir at a high formation pressure and further improving the shale gas seepage capacity. Micro-fracture is the main seepage channel of shale reservoirs and greatly improves their seepage conditions.

4.3. Influence of Crack Size on the Distribution Rate. Figure 4 shows the weighting coefficient and pressure relationships under different fracture geometry conditions. It can be found from Figure 4 that (a) macroscale fractures are the main factors controlling shale gas enrichment and seepage. Macroscale fractures are usually associated with geological faults and interconnected to form a fracture system or generated by artificial hydraulic fracturing. The fracture system can form a channel for shale gas loss and cause damage to shale gas reservoirs. In addition, even if it is not connected with the fracture system, macroscale fractures can penetrate the entire shale interval, making the vertical permeability of shale increase. If the seepage channel formed can communicate with the high

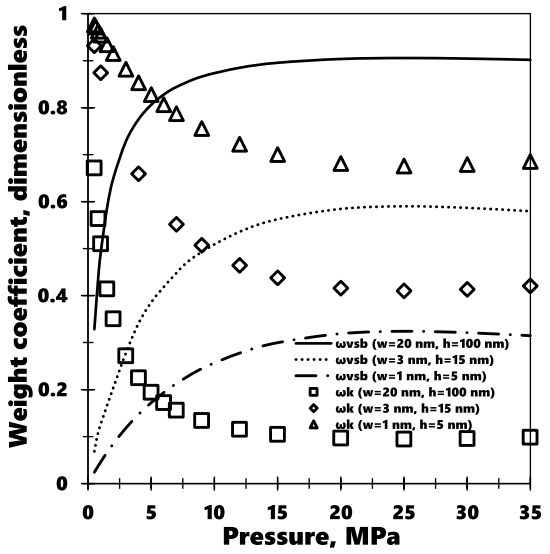

Figure 4. Relationship between the weighting coefficient and the pressure under different fracture geometry conditions.

permeability layer in the roof and floor, it can also cause the shale gas to migrate outward and reduce the gas content. The development intensity of the primary fracture network system has a significant negative correlation with the daily gas production of a single well. The greater the development intensity of the primary fracture network system, the lower the gas production of a single well, which is different from the fracture network formed by artificial hydraulic fracturing. (b) Mesoscale fractures are important factors controlling the occurrence and seepage of shale gas. Mesoscale fractures can connect the interior and exterior of shale reservoirs, have strong gas migration ability, and are the dominant channel of shale gas seepage, which is easy to cause shale gas loss and is not conducive to reservoir formation. In areas with weak structures, mesoscale fractures are the main cause of shale gas loss and the key to control shale gas productivity. In areas with large dip angles, the development scale and degree of fractures are large, which control the lateral migration of shale gas and are the main cause of shale gas loss. (c) Small-scale fractures can effectively communicate micro-fractures and medium-fractures in shale reservoirs and enable shale gas to migrate from local high pressure to low pressure for a short distance. The fracture opening of small-scale fractures decreases with the increase of permeability and burial depth.

4.4. Influence of the Methane Content on the Transmission Rate. Figure 5 shows the relationship between mass flow rates of different seepage mechanisms and pressure under different fracture width and height conditions. It can be found from Figure 5 that (a) different types of gas molecules have similar transport mechanisms, but their transfer mechanisms are affected by the coupling control of "molecular mass—molecular diameter—free path—temperature—pressure". (b) Macroscale fractures are developed in the range of shale series; mesoscale fractures are developed in a single lithofacies shale; small-scale fractures are developed in the shale laminae; and microscale fractures are developed in the shale laminae. (c) The rock mechanical layer controls the formation. The changes of the rock mechanical layer and its interface in different geological periods and under different geological conditions control the formation of natural fractures of different scales.

https://doi.org/10.1021/acsomega.3c01391
ACS Omega 2023, 8, 17077−17085

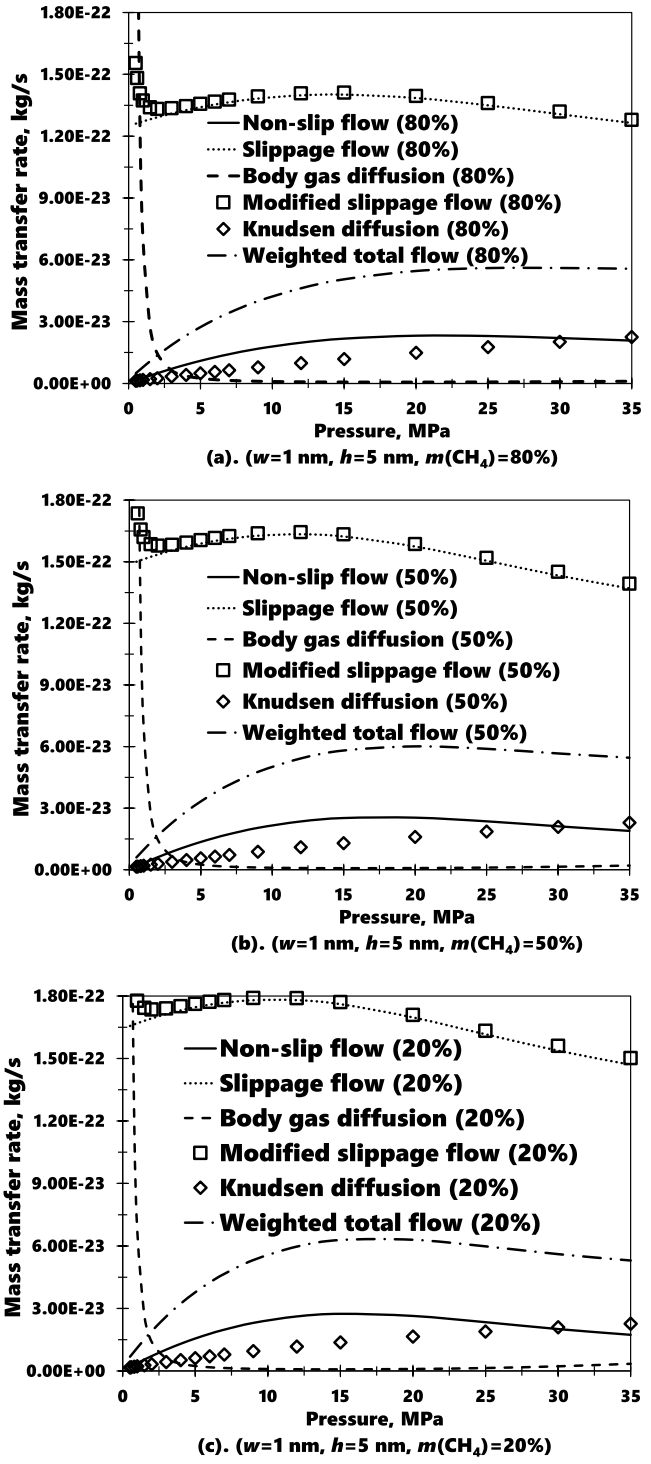

Figure 5. Relationship between mass flow rates of different seepage mechanisms and pressure under different fracture width and height conditions.

4.5. Strength and Limitations of the Model. The strength of the model:

(a) The model considers the microscale effect and mixed gas effect of high-temperature and high-pressure gas in shale gas reservoirs.
(b) The model uses comparative pressure instead of actual pressure.
(c) The model considers the real gas effect under high temperature and pressure conditions.
(d) The model has modified the viscosity equation, average molecular free path equation, and Knudsen equation under mixed gas conditions.
(e) The model considers the geometric characteristics of microscale fractures.
(f) The continuous flow equation, slippage flow equation, bulk gas diffusion equation, and Knudsen diffusion equation are coupled in the model;
(g) The model is an analytical model that has the characteristics of accurate, fast, and low economic cost, making it suitable for numerical simulation calculations.

Limitations of the model:

In this paper, the *z*-factor, viscosity, and density of gas mixture equations are calculated on the basis of previous studies.[19−22,24,31,45,48,55,67,68,70,74,78,80−88] In the future, this model will be further validated with experimental data.

5. CONCLUSIONS

Shale gas reservoirs are rich in microscale fractures. When the shale reservoir is fractured, the internal gas first enters the main fracture through the fracture. Therefore, studying the flow of gas in microscale fractures is a bridge connecting matrix seepage and artificial fracture seepage. Through mathematical model research, the following conclusions are obtained:

(a) As the pressure increases, the actual gas effect of the mixed gas at the initial stage is not obvious, and when the pressure exceeds 20 MPa, the actual gas effect of the mixed gas cannot be ignored.
(b) After considering the slip flow of the solid surface, the mass flow rate of multi-component gas under different pressure conditions increases by about 20−10,000%.
(c) Different from continuous flow and slip flow, the mass flow rate of bulk gas diffusion decreases with pressure. The mass flow rate of bulk gas diffusion decreased from 4×10^{-22} to 1.08×10^{-24} kg/s.
(d) Bulk gas diffusion mechanism of multi-component mixed gas should be considered.

APPENDIX A

In actual shale reservoirs, methane is in a high-temperature and high-pressure state. Therefore, it is necessary to modify the gas state equation. The compressibility factor is widely used in the petroleum industry and can be expressed as eqs A-1−A-3.[80,81] In addition, the viscosity, average molecular free path, Knudsen number, fracture geometry, and other parameters of mixed gas in shale reservoir need to be characterized. The relevant analytical expressions are shown below.[82−90]

$$Z_i = 1 + \frac{P_{ri}}{10.24T_{ri}}\left[2.16\frac{1}{T_{ri}}\left(\frac{1}{T_{ri}} + 1\right) - 1\right] \quad \text{(A-1)}$$

$$P_{ri} = \frac{P}{P_{ci}} \quad \text{(A-2)}$$

$$T_{ri} = \frac{T}{T_{ci}} \quad \text{(A-3)}$$

$$Z_{mixture} = m_1Z_1 + m_2Z_2 + \cdots + m_iZ_i + \cdots + m_{n-1}Z_{n-1} + m_nZ_n \quad \text{(A-4)}$$

https://doi.org/10.1021/acsomega.3c01391
ACS Omega 2023, 8, 17077−17085

$$\mu_{\text{real},i} = \mu_i\left[1 + \frac{A_1}{T_{\text{ri}}^5}\frac{p_{\text{ri}}^4}{T_{\text{ri}}^{20} + P_{\text{ri}}^4} + A_2\left(\frac{P_{\text{ri}}}{T_{\text{ri}}}\right)^2 + A_3\frac{P_{\text{ri}}}{T_{\text{ri}}}\right] \quad \text{(A-5)}$$

$$\mu_{\text{real,mixture}} = m_1\mu_{\text{real},1} + m_2\mu_{\text{real},2} + \cdots + m_i\mu_{\text{real},i} + \cdots + m_{n-1}\mu_{\text{real},n-1} + m_n\mu_{\text{real},n} \quad \text{(A-6)}$$

$$\lambda_{\text{real},i} = \frac{\mu_{\text{real},i}}{P}\sqrt{\frac{\pi Z_i RT}{2M_i}} \quad \text{(A-7)}$$

$$\lambda_{\text{real,mixture}} = m_1\lambda_{\text{real},1} + m_2\lambda_{\text{real},2} + \cdots + m_i\lambda_{\text{real,i}} + \cdots + m_{n-1}\lambda_{\text{real},n-1} + m_n\lambda_{\text{real},n} \quad \text{(A-8)}$$

$$M_{\text{real,mixture}} = m_1M_{\text{real},1} + m_2M_{\text{real},2} + \cdots + m_iM_{\text{real,i}} + \cdots + m_{n-1}M_{\text{real},n-1} + m_nM_{\text{real},n} \quad \text{(A-9)}$$

$$Kn_{\text{real},i} = \frac{\lambda_{\text{real},i}}{r_{\text{equivalent}}} \quad \text{(A-10)}$$

$$Kn_{\text{real,mixture}} = m_1Kn_{\text{real},1} + m_2Kn_{\text{real},2} + \cdots + m_iKn_{\text{real},i} + \cdots + m_{n-1}Kn_{\text{real},n-1} + m_nKn_{\text{real},n} \quad \text{(A-11)}$$

$$\varsigma = w/h \quad \text{(A-12)}$$

$$Kn = \lambda/h \quad \text{(A-13)}$$

$$\lambda = \frac{\mu}{p}\sqrt{\frac{\pi RT}{2M}} \quad \text{(A-14)}$$

$$Kn = \frac{\lambda}{r_{\text{equivalent}}} \quad \text{(A-15)}$$

where Z_i is the compressibility factor of ith gas under the condition of high temperature and pressure, dimensionless; P_{ri} and T_{ri} are contrastive pressure and temperature, Pa & K, respectively; P_{ci} and T_{ci} are critical pressure and temperature, Pa & K, respectively; Z_{mixture} is the compressibility factor of shale mixed gas under the condition of high temperature and pressure, dimensionless; $\mu_{\text{real},i}$ is the gas viscosity under the condition of high temperature and pressure, Pa·s; $\mu_{\text{real,mixture}}$ represents the gas mixture viscosity under the condition of high temperature and pressure, Pa·s; $\lambda_{\text{real},i}$ represents an average molecular free path of ith gas under the condition of high temperature and pressure, m; $\lambda_{\text{real,mixture}}$ is an average molecular free path of gas mixture under the condition of high temperature and pressure, m; $Kn_{\text{real},i}$ is the Knudsen number under the condition of high temperature and pressure, dimensionless; $Kn_{\text{real,mixture}}$ is the Knudsen number of gas mixture under the condition of high temperature and pressure, dimensionless; and $r_{\text{equivalent}}$ is an equivalent radius, m.

Based on the basic equations above, the modified slip flow can be modeled as

$$J_{\text{v,real}} = -A(\varsigma)\frac{\phi}{\tau}\frac{wh^3}{12\mu_{\text{real,mixture}}}\frac{pM_{\text{mixture}}}{Z_{\text{mixture}}RT}\frac{\text{d}P}{\text{d}l} \quad \text{(A-16)}$$

Conductivity

$$C_{\text{v,real}} = -A(\varsigma)\frac{\phi}{\tau}\frac{wh^3}{12\mu_{\text{real,mixture}}}\frac{pM_{\text{mixture}}}{Z_{\text{mixture}}RT} \quad \text{(A-17)}$$

Due to the gravitational attraction of methane and other gases on the shale wall, some gases are adsorbed on the shale surface. The transport of these adsorbed gases to shale gas cannot be ignored. The following equation can be expressed as

$$J_{\text{vs,real}} = -A(\varsigma)\frac{\phi}{\tau}\frac{wh^3}{12\mu_{\text{real,mixture}}}\frac{pM_{\text{mixture}}}{Z_{\text{mixture}}RT}(1 + \alpha Kn_{\text{real,mixture}})\left(1 + \frac{6Kn_{\text{real,mixture}}}{1 - bKn_{\text{real,mixture}}}\right)\frac{\text{d}P}{\text{d}l} \quad \text{(A-18)}$$

Conductivity

$$C_{\text{vs,real}} = -A(\varsigma)\frac{\phi}{\tau}\frac{wh^3}{12\mu_{\text{real,mixture}}}\frac{pM_{\text{mixture}}}{Z_{\text{mixture}}RT}(1 + \alpha Kn_{\text{real,mixture}})\left(1 + \frac{6Kn_{\text{real,mixture}}}{1 - bKn_{\text{real,mixture}}}\right) \quad \text{(A-19)}$$

In summary, the analytical equation for microscale gas transport in high-temperature and high-pressure environments can be expressed as

$$J_{\text{b,real}} = -\frac{1}{3}\varsigma\lambda_{\text{real,mixture}}\sigma^{D_f-2}\left(\frac{8ZM_{\text{mixture}}}{\pi RT}\right)^{0.5}\frac{P}{Z_{\text{mixture}}}C_{\text{g}}\frac{\text{d}P}{\text{d}L} \quad \text{(A-20)}$$

$$C_{\text{g}} = \frac{1}{P} - \frac{1}{Z_{\text{mixture}}}\frac{\text{d}Z_{\text{mixture}}}{\text{d}P} \quad \text{(A-21)}$$

Conductivity

$$C_{\text{b,real}} = \frac{1}{3}\varsigma\lambda_{\text{real,mixture}}\sigma^{D_f-2}\left(\frac{8ZM_{\text{mixture}}}{\pi RT}\right)^{0.5}\frac{P}{Z_{\text{mixture}}}C_{\text{g}} \quad \text{(A-22)}$$

On this basis, the detachment diffusion on the surface of shale microcracks can be expressed as

$$J_{\text{vsb,real}} = -A(\varsigma)\frac{\phi}{\tau}\frac{wh^3}{12\mu_{\text{real,mixture}}}\frac{pM_{\text{mixture}}}{Z_{\text{mixture}}RT}(1 + \alpha Kn_{\text{real,mixture}})\left(1 + \frac{6Kn_{\text{real,mixture}}}{1 - bKn_{\text{real,mixture}}}\right)\frac{\text{d}P}{\text{d}l} + \frac{1}{Kn_{\text{real,mixture}}}\left(-\frac{1}{3}\varsigma\lambda_{\text{real,mixture}}\sigma^{D_f-2}\left(\frac{8ZM_{\text{mixture}}}{\pi RT}\right)^{0.5}\frac{P}{Z_{\text{mixture}}}C_{\text{g}}\frac{\text{d}P}{\text{d}L}\right) \quad \text{(A-23)}$$

Conductivity

https://doi.org/10.1021/acsomega.3c01391
ACS Omega 2023, 8, 17077−17085

$$C_{vsb,real} = -A(\varsigma)\frac{\phi}{\tau}\frac{wh^3}{12\mu_{real,mixture}}\frac{pM_{mixture}}{Z_{mixture}RT}(1 + \alpha Kn_{real,mixture})\left(1 + \frac{6Kn_{real,mixture}}{1 - bKn_{real,mixture}}\right) + \frac{1}{Kn_{real,mixture}}\left(-\frac{1}{3}\varsigma\lambda_{real,mixture}\sigma^{D_f-2}\left(\frac{8ZM_{mixture}}{\pi RT}\right)^{0.5}\frac{P}{Z_{mixture}}C_g\right) \quad \text{(A-24)}$$

Finally, the above equations are coupled with Knudsen flow to obtain eqs 1 and 2.

AUTHOR INFORMATION

Corresponding Author

Jiangtao Li − *Key Laboratory of Continental Shale Hydrocarbon Accumulation and Efficient Development (Northeast Petroleum University), Ministry of Education, Northeast Petroleum University, Daqing 163318 Heilongjiang, China; Institute of Unconventional Oil & Gas, Northeast Petroleum University, Daqing 163318, China;* orcid.org/0000-0003-3225-2627; Email: lijiangtao112@163.com

Authors

Ying Yang − *Key Laboratory of Continental Shale Hydrocarbon Accumulation and Efficient Development (Northeast Petroleum University), Ministry of Education, Northeast Petroleum University, Daqing 163318 Heilongjiang, China; Institute of Unconventional Oil & Gas, Northeast Petroleum University, Daqing 163318, China*

Xin Zhang − *Geology Party of the Third Oil Production Plant, Daqing Oilfield, Daqing 163318, China*

Xiaofeng Zhou − *Key Laboratory of Continental Shale Hydrocarbon Accumulation and Efficient Development (Northeast Petroleum University), Ministry of Education, Northeast Petroleum University, Daqing 163318 Heilongjiang, China; Institute of Unconventional Oil & Gas, Northeast Petroleum University, Daqing 163318, China*

Anlun Wang − *Key Laboratory of Continental Shale Hydrocarbon Accumulation and Efficient Development (Northeast Petroleum University), Ministry of Education, Northeast Petroleum University, Daqing 163318 Heilongjiang, China; Institute of Unconventional Oil & Gas, Northeast Petroleum University, Daqing 163318, China*

Complete contact information is available at: https://pubs.acs.org/10.1021/acsomega.3c01391

Notes

The authors declare no competing financial interest.

ACKNOWLEDGMENTS

This work was supported by the Natural Science Foundation of Heilongjiang Province of China (grant no. LH2021E014), the Guiding Science and Technology Planning Project of Daqing (grant no. zd-2021-36), the Postdoctoral Scientific Research Developmental Fund of Heilongjiang Province, China (grant no. LBH-Z21084), the Natural Science Foundation of Heilongjiang Province (grant no. LH2022E019), and the China Postdoctoral Science Foundation (grant no. 2022M710594).

REFERENCES

(1) Zhu, H. J.; Ju, Y. W.; Huang, C.; Chen, F. W.; Chen, B. Z.; Yu, K. Microcosmic gas adsorption mechanism on clay-organic nanocomposites in a marine shale. *Energy* **2020**, *197*, 117256.

(2) Guo, Y. H.; Liu, F.; Qiu, J. J.; Xu, Z.; Bao, B. Microscopic transport and phase behaviors of CO_2 injection in heterogeneous formations using microfluidics. *Energy* **2022**, *256*, 124524.

(3) Cao, G. H.; Jiang, W. B.; Lin, M.; Ji, L.; Xu, Z.; Zheng, S.; Hao, F. Mortar dynamic coupled model for calculating interface gas exchange between organic and inorganic matters of shale. *Energy* **2021**, *236*, 121449.

(4) Yang, H.; Han, X.; Wang, L. Is there a bubble in the shale gas market? *Energy* **2021**, *215*, 119101.

(5) Gao, F.; Xie, H.; Xie, L.; Yang, Y.; Ju, Y.; Wang, J. Novel idea of the theory and application of 3D volume fracturing for stimulation of shale gas reservoirs. *Chin. Sci. Bull.* **2016**, *61*, 36−46.

(6) Garratt, A.; Petrella, I.; Zhang, Y. Y. Asymmetry and interdependence when evaluating U.S. Energy Information Administration forecasts. *Energy Econ.* **2023**, *121*, 106620.

(7) Yao, J.; Sun, H.; Huang, C. Q. Key mechanical problems in the developmentof shale gas reservoirs. *Sci. China: Phys., Mech. Astron.* **2013**, *12*, 1527−1547.

(8) Liu, J.; Xue, Y.; Fu, Y.; Yao, K.; Liu, J. Numerical investigation on microwave-thermal recovery of shale gas based on a fully coupled electromagnetic, heat transfer, and multiphase flow model. *Energy* **2023**, *263*, 126090.

(9) Bilgen, S.; Sarıkaya, İ. New horizon in energy: Shale gas. *J. Nat. Gas Sci. Eng.* **2016**, *35*, 637−645.

(10) Yang, J. H.; Wang, M.; Wu, L.; Liu, Y.; Qiu, S.; Xu, P. A novel Monte Carlo simulation on gas flow in fractal shale reservoir. *Energy* **2021**, *236*, 121513.

(11) Yang, X.; Zhou, W. N.; Liu, X. L.; Yan, Y. A multiscale approach for simulation of shale gas transport in organic nanopores. *Energy* **2020**, *210*, 118547.

(12) Liu, B.; Sun, J.; Zhang, Y.; He, J.; Fu, X.; Yang, L.; Xing, J.; Zhao, X. Reservoir space and enrichment model of shale oil in the first member of Cretaceous Qingshankou Formation in the Changling sag, southern Songliao Basin, NE China. *Pet. Explor. Dev.* **2021**, *48*, 608−624.

(13) Liu, B.; Song, Y.; Zhu, K.; Su, P.; Ye, X.; Zhao, W. Mineralogy and element geochemistry of salinized lacustrine organic-rich shale in the Middle Permian Santanghu Basin: Implications for paleoenvironment, provenance, tectonic setting and shale oil potential. *Mar. Pet. Geol.* **2020**, *120*, 104569.

(14) Pan, Z.; Connell, L. D. Reservoir simulation of free and adsorbed gas production from shale. *J. Nat. Gas Sci. Eng.* **2015**, *22*, 359−370.

(15) Liu, B.; Wang, H.; Fu, X.; Bai, Y.; Bai, L.; Jia, M.; He, B. Lithofacies and depositional setting of a highly prospective lacustrine shale oil succession from the Upper Cretaceous Qingshankou Formation in the Gulong Sag, northern Songliao Basin, Northeast China. *AAPG Bull.* **2019**, *103*, 405−432.

(16) Jia, D. *Research on Nonlinear Seepage Theory of Multistage Fractured Horizontal Wells in Shale Gas Reservoir*; University of Science and Technology Beijing, 2015.

(17) Zou, C. N.; Zhu, R. K.; Bai, B. The first discovery of nanoscale pores in oil and gas reservoirs in China and their scientific value. *Acta Petrol. Sin.* **2011**, *6*, 1857−1864.

(18) Zhu, W. Y.; Qi, Q. Research on the multi-scale and complex flow mechanism and model of shale gas. *Sci. China: Technol. Sci.* **2016**, *2*, 111−119.

(19) Javadpour, F. Nanopores and Apparent Permeability of Gas Flow in Mudrocks (Shales and Siltstone). *J. Can. Pet. Technol.* **2009**, *48*, 16−21.

(20) Wu, K. L.; Li, X. F.; Chen, Z. X. Nanopore gas transport model for shale gas. *Acta Pet. Sin.* **2015**, *36*, 837−848.

(21) Chen, M. J.; Kang, Y. L.; Zhang, T. S.; Chen, Z.; Wu, K. Characteristics of multiscale mass transport and coordination mechanisms for shale gas. *Sci. China: Technol. Sci.* **2018**, *48*, 473−487.
(22) Javadpour, F.; Fisher, D.; Unsworth, M. Nanoscale gas flow in shale gas sediments. *J. Can. Pet. Technol.* **2007**, *46*, 55−61.
(23) Wang, Y.; Pu, J.; Wang, L.; Wang, J.; Jiang, Z.; Song, Y. F.; Wang, C. C.; Wang, Y.; Jin, C. Characterization of typical 3D pore networks of Jiulaodong formation shale using nano-transmission X-ray microscopy. *Fuel* **2016**, *170*, 84−91.
(24) Yang, F.; Ning, Z.; Liu, H. Fractal characteristics of shales from a shale gas reservoir in the Sichuan Basin, China. *Fuel* **2014**, *115*, 378−384.
(25) Zhuang, Z.; Liu, Z. L.; Wang, Y. L. Fundamental theories and key mechanical issues in the efficient development of shale oil and gas. *Q. Mech.* **2015**, No. 1, 11−25.
(26) Liu, J. Study on Shale Gas Multi-scale Transport Characteristics and Flow Consistency Mechanism. Doctoral Dissertation, China University of Mining and Technology, Xuzhou, 2019.
(27) Chalmers, G. R. L.; Bustin, R. M. The organic matter distribution and methane capacity of the Lower Cretaceous strata of Northeastern British Columbia, Canada. *Int. J. Coal Geol.* **2007**, *70*, 223−239.
(28) Gasparik, M.; Ghanizadeh, A.; Bertier, P.; Gensterblum, Y.; Bouw, S.; Krooss, B. M. High-Pressure Methane Sorption Isotherms of Black Shales from The Netherlands. *Energy Fuels* **2012**, *26*, 4995−5004.
(29) Loucks, R. G.; Reed, R. M.; Ruppel, S. C.; Jarvie, D. M. Morphology, Genesis, and Distribution of Nanometer-Scale Pores in Siliceous Mudstones of the Mississippian Barnett Shale. *J. Sediment. Res.* **2009**, *79*, 848−861.
(30) Clarkson, C. R.; Jensen, J. L.; Pedersen, P. K.; Freeman, M. Innovative methods for flow-unit and pore-structure analyses in a tight siltstone and shale gas reservoir. *AAPG Bull.* **2012**, *96*, 355−374.
(31) Ross, D. J. K.; Marc Bustin, R. The importance of shale composition and pore structure upon gas storage potential of shale gas reservoirs. *Mar. Pet. Geol.* **2009**, *26*, 916−927.
(32) Zhang, T.; Ellis, G. S.; Ruppel, S. C.; Milliken, K.; Yang, R. Effect of organic-matter type and thermal maturity on methane adsorption in shale-gas systems. *Org. Geochem.* **2012**, *47*, 120−131.
(33) Wang, S.; Song, Z.; Cao, T.; Song, X. The methane sorption capacity of Paleozoic shales from the Sichuan Basin, China. *Mar. Pet. Geol.* **2013**, *44*, 112−119.
(34) Wang, Y.; Zhu, Y.; Liu, S.; Zhang, R. Methane adsorption measurements and modeling for organic-rich marine shale samples. *Fuel* **2016**, *172*, 301−309.
(35) Chen, J.; Wang, F.; Liu, H.; Wu, H. Molecular mechanism of adsorption/desorption hysteresis: dynamics of shale gas in nanoscale pores. *Sci. China: Phys., Mech. Astron.* **2017**, *60*, 014611.
(36) Zhao, T.; Li, X.; Zhao, H.; Li, M. Molecular simulation of adsorption and thermodynamic properties on type II kerogen: Influence of maturity and moisture content. *Fuel* **2017**, *190*, 198−207.
(37) Li, J.; Ma, Y.; Huang, K.; Lu, S.; Yin, J.; Zhang, Y. Comprehensive polynomial simulation and prediction for Langmuir volume and Langmuir pressure of shale gas adsorption using multiple factors. *Mar. Pet. Geol.* **2017**, *88*, 1004−1012.
(38) Chen, M.; Kang, Y.; Zhang, T.; Li, X.; Wu, K.; Chen, Z. Methane adsorption behavior on shale matrix at in-situ pressure and temperature conditions: Measurement and modeling. *Fuel* **2018**, *228*, 39−49.
(39) Bustin, R. M.; Clarkson, C. R. Geological controls on coalbed methane reservoir capacity and gas content. *Int. J. Coal Geol.* **1998**, *38*, 3−26.
(40) Chalmers, G. R. L.; Bustin, R. M. Lower Cretaceous gas shales in northeastern British Columbia, Part II: evaluation of regional potential gas resources. *Bull. Can. Pet. Geol.* **2008**, *56*, 22−61.
(41) Wang, S.; Song, Z.; Cao, T.; Song, X. The methane sorption capacity of Paleozoic shales from the Sichuan Basin, China. *Mar. Pet. Geol.* **2013**, *44*, 112−119.
(42) Ji, L.; Zhang, T.; Milliken, K. L.; Qu, J.; Zhang, X. Experimental investigation of main controls to methane adsorption in clay-rich rocks. *Appl. Geochem.* **2012**, *27*, 2533−2545.
(43) Clarkson, C. R.; Solano, N.; Bustin, R. M.; Bustin, A.; Chalmers, G.; He, L.; Melnichenko, Y.; Radliński, A.; Blach, T. Pore structure characterization of North American shale gas reservoirs using USANS/SANS, gas adsorption, and mercury intrusion. *Fuel* **2013**, *103*, 606−616.
(44) Shi, M.; Yu, B.; Xue, Z.; Wu, J.; Yuan, Y. Pore characteristics of organic-rich shales with high thermal maturity: A case study of the Longmaxi gas shale reservoirs from well Yuye-1 in southeastern Chongqing, China. *J. Nat. Gas Sci. Eng.* **2015**, *26*, 948−959.
(45) Chalmers, G. R.; Bustin, R. M.; Power, I. M. Characterization of gas shale pore systems by porosimetry, pycnometry, surface area, and field emission scanning electron microscopy/transmission electron microscopy image analyses: Examples from the Barnett, Woodford, Haynesville, Marcellus, and Doig units. *AAPG Bull.* **2012**, *96*, 1099−1119.
(46) Liang, L.; Xiong, J.; Liu, X. An investigation of the fractal characteristics of the Upper Ordovician Wufeng Formation shale using nitrogen adsorption analysis. *J. Nat. Gas Sci. Eng.* **2015**, *27*, 402−409.
(47) Loucks, R. G.; Reed, R. M.; Ruppel, S. C.; Hammes, U. Spectrum of pore types and networks in mudrocks and a descriptive classification for matrix-related mudrock pores. *AAPG Bull.* **2012**, *96*, 1071−1098.
(48) Yang, F.; Ning, Z. F.; Hu, C. P. Microscopic pore structure characteristics of shale reservoirs. *Acta Pet. Sin.* **2013**, *34* (2), 301−311.
(49) Cao, T.; Song, Z.; Wang, S.; Xia, J. Characterization of pore structure and fractal dimension of Paleozoic shales from the northeastern Sichuan Basin, China. *J. Nat. Gas Sci. Eng.* **2016**, *35*, 882−895.
(50) Bu, H.; Ju, Y.; Tan, J.; Wang, G.; Li, X. Fractal characteristics of pores in non-marine shales from the Huainan coalfield, eastern China. *J. Nat. Gas Sci. Eng.* **2015**, *24*, 166−177.
(51) Liu, X.; Xiong, J.; Liang, L. Investigation of pore structure and fractal characteristics of organic-rich Yanchang formation shale in central China by nitrogen adsorption/desorption analysis. *J. Nat. Gas Sci. Eng.* **2015**, *22*, 62−72.
(52) Tang, X.; Jiang, Z.; Li, Z.; Gao, Z.; Bai, Y.; Zhao, S.; Feng, J. The effect of the variation in material composition on the heterogeneous pore structure of high-maturity shale of the Silurian Longmaxi formation in the southeastern Sichuan Basin, China. *J. Nat. Gas Sci. Eng.* **2015**, *23*, 464−473.
(53) Sakhaee-Pour, A.; Bryant, S. L. Pore structure of shale. *Fuel* **2015**, *143*, 467−475.
(54) Sun, H.; Yao, J.; Cao, Y.; Fan, D. y.; Zhang, L. Characterization of gas transport behaviors in shale gas and tight gas reservoirs by digital rock analysis. *Int. J. Heat Mass Transfer* **2017**, *104*, 227−239.
(55) Sun, H. *Multi-scale flow simulation theory and method for shale gas reservoirs*; China University of Petroleum: East China, 2013.
(56) Hou, P. *Study on the mechanism of gas pressure fracturing and anti-reflection effect of low-permeability reservoir rocks*; China University of Mining and Technology, 2018.
(57) Deng, J.; Zhu, W.; Ma, Q. A new seepage model for shale gas reservoir and productivity analysis of fractured well. *Fuel* **2014**, *124*, 232−240.
(58) Dongari, N.; Sharma, A.; Durst, F. Pressure-driven diffusive gas flows in micro-channels: from the Knudsen to the continuum regimes. *Microfluid. Nanofluid.* **2009**, *6*, 679−692.
(59) Veltzke, T.; Thöming, J. An analytically predictive model for moderately rarefied gas flow. *J. Fluid Mech.* **2012**, *698*, 406−422.
(60) Roy, S.; Raju, R.; Chuang, H. F.; Cruden, B. A.; Meyyappan, M. Modeling gas flow through microchannels and nanopores. *J. Appl. Phys.* **2003**, *93*, 4870−4879.
(61) Klinkenberg, L. J. The permeability of porous media to liquids and gases. *Drilling and Production Practice*; American Petroleum Inst., 1941; pp 200−213.
(62) Beskok, A.; Karniadakis, G. E. Report: a model for flows in channels, pipes, and ducts at micro and nano scales. *Microscale Thermophys. Eng.* **1999**, *3*, 43−77.
(63) Civan, F. Effective Correlation of Apparent Gas Permeability in Tight Porous Media. *Transp. Porous Media* **2010**, *82*, 375−384.

https://doi.org/10.1021/acsomega.3c01391
ACS Omega 2023, 8, 17077−17085

(64) Zhu, W.-Y.; Ma, Q.; Deng, J. Mathematical model and application of gas flow in nano-micron pores. *J. Univ. Sci. Technol. Beijing* **2014**, *36*, 709−715.
(65) Darabi, H.; Ettehad, A.; Javadpour, F.; Sepehrnoori, K. Gas flow in ultra-tight shale strata. *J. Fluid Mech.* **2012**, *710*, 641−658.
(66) Singh, H.; Javadpour, F.; Ettehadtavakkol, A.; Darabi, H. Nonempirical Apparent Permeability of Shale. *SPE Reservoir Eval. Eng.* **2014**, *17*, 414−424.
(67) Wu, K.; Li, X.; Wang, C. Apparent Permeability for Gas Flow in Shale Reservoirs Coupling Effects of Gas Diffusion and Desorption. *Unconventional Resources Technology Conference*, 2014.
(68) Xiong, X.; Devegowda, D.; Villazon, G. A Fully-Coupled Free and Adsorptive Phase Transport Model for Shale Gas Reservoirs Including Non-Darcy Flow Effects. *SPE Annual Technical Conference and Exhibition*, 2012.
(69) Wu, K.; Li, X.; Wang, C.; Yu, W.; Chen, Z. Model for Surface Diffusion of Adsorbed Gas in Nanopores of Shale Gas Reservoirs. *Ind. Eng. Chem. Res.* **2015**, *54*, 3225−3236.
(70) Wang, J.; Liu, H.; Wang, L.; Zhang, H.; Luo, H.; Gao, Y. Apparent permeability for gas transport in nanopores of organic shale reservoirs including multiple effects. *Int. J. Coal Geol.* **2015**, *152*, 50−62.
(71) Naraghi, M. E.; Javadpour, F. A stochastic permeability model for the shale-gas systems. *Int. J. Coal Geol.* **2015**, *140*, 111−124.
(72) Behrang, A.; Kantzas, A. A hybrid methodology to predict gas permeability in nanoscale organic materials; a combination of fractal theory, kinetic theory of gases and Boltzmann transport equation. *Fuel* **2017**, *188*, 239−245.
(73) Singh, H.; Javadpour, F. Langmuir slip-Langmuir sorption permeability model of shale. *Fuel* **2016**, *164*, 28−37.
(74) Geng, L.; Li, G.; Zitha, P.; Tian, S.; Sheng, M.; Fan, X. A diffusion−viscous flow model for simulating shale gas transport in nano-pores. *Fuel* **2016**, *181*, 887−894.
(75) Song, W.; Yao, J.; Li, Y.; Sun, H.; Zhang, L.; Yang, Y.; Zhao, J.; Sui, H. Apparent gas permeability in an organic-rich shale reservoir. *Fuel* **2016**, *181*, 973−984.
(76) Yuan, Y.; Gholizadeh Doonechaly, N.; Rahman, S. An Analytical Model of Apparent Gas Permeability for Tight Porous Media. *Transp. Porous Media* **2016**, *111*, 193−214.
(77) Kazemi, M.; Takbiri-Borujeni, A. An analytical model for shale gas permeability. *Int. J. Coal Geol.* **2015**, *146*, 188−197.
(78) Wu, K.; Chen, Z.; Li, X. Real gas transport through nanopores of varying cross-section type and shape in shale gas reservoirs. *Chem. Eng. J.* **2015**, *281*, 813−825.
(79) Ambrose, R. J.; Hartman, R. C.; Diaz-Campos, M. New pore-scale considerations for shale gas in place calculations. *SPE Unconventional Gas Conference*, 2010.
(80) Loebenstein, W. V. Calculations and comparisons of nonideal gas corrections for use in gas adsorption. *J. Colloid Interface Sci.* **1971**, *36*, 397−400.
(81) Sun, F. R.; Yao, Y. D.; Li, G. Z.; Liu, W. Y. Simulation of real gas mixture transport through aqueous nanopores during the depressurization process considering stress sensitivity. *J. Pet. Sci. Eng.* **2019**, *178*, 829−837.
(82) Qu, S. Y.; Jiang, H. Q.; Lu, C. H.; You, C. C. Shale gas production in nanoscale fractures with real gas effect. *Arabian J. Geosci.* **2020**, *13*, 1266.
(83) Ma, H. M.; Yang, Y.; Zhang, Y. M.; Li, Z.; Zhang, K.; Xue, Z.; Zhan, J.; Chen, Z. Optimized schemes of enhanced shale gas recovery by CO_2-N_2 mixtures associated with CO_2 sequestration. *Energy Convers. Manage.* **2022**, *268*, 116062.
(84) Sun, F. R.; Yao, Y. D.; Li, G. Z.; Dong, M. D. Transport behaviors of real gas mixture through nanopores of shale reservoir. *J. Pet. Sci. Eng.* **2019**, *177*, 1134−1141.
(85) Wang, Y. N.; Jin, Z. H. Hydrocarbon mixture and CO_2 adsorptions in a nanopore-bulk multiscale system in relation to CO_2 enhanced shale gas recovery. *Chem. Eng. J.* **2021**, *415*, 128398.
(86) Zhang, L.; Li, Q. B.; Liu, C.; Liu, Y.; Cai, S. Y.; Wang, S. K.; Cheng, Q. L. Molecular insight of flow property for gas-water mixture (CO_2/CH_4-H_2O) in shale organic matrix. *Fuel* **2021**, *288*, 119720.
(87) Sun, F. R.; Yao, Y. D.; Li, G. Z.; Zhang, S. K.; Xu, Z. M.; Shi, Y.; Li, X. F. A slip-flow model for oil transport in organic nanopores. *J. Pet. Sci. Eng.* **2019**, *172*, 139−148.
(88) Cihan, A.; Tokunaga, T. K.; Birkholzer, J. T. Diffusion-to-Imbibition Transition in Water Sorption in Nanoporous Media: Theoretical Studies. *Water Resour. Res.* **2021**, *57*, No. e2021WR029720.
(89) Fang, C.; Kang, Q.; Qiao, R. The Role of Disjoining Pressure and Thermal Activation in the Invasion of Droplets into Nanopores. *J. Phys. Chem. C* **2019**, *123*, 6905−6912.
(90) Fang, C.; Zhang, F.; Qiao, R. Invasion of gas into mica nanopores: a molecular dynamics study. *J. Phys.: Condens. Matter* **2018**, *30*, 224001.

https://doi.org/10.1021/acsomega.3c01391
ACS Omega 2023, 8, 17077−17085